The collinear cluster tri-partition (CCT) of ^{252}Cf (sf): New aspects from neutron gated data

Yu.V. Pyatkov, D.V. Kamanin, W. von Oertzen, A.A. Alexandrov, I.A. Alexandrova, O.V. Falomkina, N. Jacobs, N.A. Kondratjev, E.A. Kuznetsova, Yu.E. Lavrova, V. Malaza, Yu.V. Ryabov, O.V. Strekalovsky, A.N. Tyukavkin and V.E. Zhuchko

Regular Article – Experimental Physics

The collinear cluster tri-partition (CCT) of ^{252}Cf (sf): New aspects from neutron gated data

Yu.V. Pyatkov[1,2,a], D.V. Kamanin[1], W. von Oertzen[3,b], A.A. Alexandrov[1], I.A. Alexandrova[1], O.V. Falomkina[1,4], N. Jacobs[5], N.A. Kondratjev[1], E.A. Kuznetsova[1,c], Yu.E. Lavrova[2], V. Malaza[5], Yu.V. Ryabov[6], O.V. Strekalovsky[1], A.N. Tyukavkin[2], and V.E. Zhuchko[1]

[1] Joint Institute for Nuclear Research, 141980 Dubna, Moscow Region, Russia
[2] National Nuclear Research University MEPHI, 115409 Moscow, Russia
[3] Helmholtz-Zentrum Berlin, Glienickerstr. 100, 14109 Berlin, Germany
[4] Lomonosov Moscow State University, Physics Faculty, Computer Methods in Physics Division, 119899, Russia
[5] University of Stellenbosch, Faculty of Military Science, Military Academy, Saldanha 7395, South Africa
[6] Institute for Nuclear Research RAN, 117312 Moscow, Russia

Abstract. Results of two different experiments for the study of fission of ^{252}Cf (sf) events in coincidence with neutrons are reported. Two time-of-flight–energy (TOF-E) detectors systems have been used. The fission fragment masses were obtained in a double arm coincidence set-up, where the missing mass in the binary decay is used to characterise ternary fission as a collinear cluster tri-partition (CCT). The ^{3}He filled neutron counters have been arranged so as to detect principally neutrons emitted from an isotropic source in the laboratory frame. The fission events connected to the larger experimental neutron multiplicities show a wide range in the missing-mass spectrum, down to α-particles, carbon and oxygen isotopes. These are linked with magic nuclei in the binary mass-mass correlations of the fission fragments. These neutron gated data are virtually free from background events from scattered binary fission fragments. The ungated spectra are compared to those of the previous data from our previous article (Eur. Phys. J. A. **45**, 29 (2010)), the observed structures agree well with the manifestations of the collinear cluster tri-partition of ^{252}Cf (sf) observed earlier. Several new families of the CCT modes are observed.

1 Introduction

The present paper is a follow-up of our previous article [1] devoted to the observation of a new kind of ternary fission decay of low-excited heavy nuclei in ^{252}Cf (sf) and in ^{235}U(n_{th}, f). This decay mode has been called by us "collinear cluster tri-partition" (CCT) in view of the observed features of the effect, that the decay partners fly apart almost collinearly and at least one of them has magic nucleon composition. A brief review of both experimental and theoretical activities in the past in the field of CCT has been presented in this article. We want to refer here on very recent theoretical articles not mentioned earlier, devoted to unusual ternary decays of heavy nuclei including CCT [2–5]. The authors analyze the potential energy of different pre-scission configurations leading to ternary

decays, and the kinetic energies of the CCT partners [6] are calculated for a sequential decay process. These results obtained, being model dependent can be considered as the first step in the description of the CCT process.

Interesting ideas for further studying of the CCT process can be inferred from [7,8] where ternary fission has been observed with lighter compound nuclei (CN) at high excitation energy and high angular momentum for ^{60}Zn* and ^{56}Fe*, respectively. The CN are formed in binary reactions (*e.g.*, ^{32}S + ^{24}Mg $\rightarrow$ ^{56}Fe) and binary decays are registered. Events of ternary decays with missing α-particles, namely 2α, 3α and 4α's, are possible, because of the larger moments of inertia of the hyperdeformed CN in the ternary decay. At higher angular momenta the fission barrier for the ternary decay becomes comparable or even lower relative to that for binary fission. A similar phenomenon should be observed in the CCT decay in heavy nuclei like in the present case. If heavy compound nuclei are populated in nuclear reactions, a considerable angular momentum is introduced. As in the cited case, the moments of inertia of the two initial configurations for binary

---

[a] e-mail: yvp_nov@mail.ru
[b] *Also at*: Fachbereich Physik, Freie Universität, Berlin, Germany
[c] e-mail: kuzena@jinr.ru

and ternary decays will give a changed relative position of the two fission barriers. For the ternary configuration the larger moment of inertia gives a relatively lower barrier for the ternary decay. A strong enhancement of the CCT decay relative to binary fission can be expected. This will be treated in an upcoming publication [9].

We would like to emphasize that, at the early stage of our work, the process of "true ternary fission" (fission of the nucleus into three fragments of comparable masses) was considered to be undiscovered for low-excited heavy nuclei [10]. Another possible prototype —three body cluster radioactivity— was also unknown. The closest process to the CCT phenomenon, at least cinematically, is the so-called "polar emission" [11], but only very light ions (up to isotopes of Be) have been observed so far. In the analysis of the experiments devoted to the "polar emission", we came to the conclusion that typical CCT fission fragments could not be detected in the cited [12] works. In fact, dE-E telescopes (energy-loss, energy) were used to stop the fission fragments (FFs) in the dE-detector located on the path of the light charged particles (LCP) flying in the same direction (polar LCP). At the same time this detector must be thin enough to be transparent for the LCP under study. The thickness of the dE-detectors, chosen as a compromise, puts a boundary for the mass/charge of the LCP, which could be detected. In order to reveal true ternary decays with almost collinear emission of the fragments, we have used different experimental approaches, which are, once more, presented in sect. 2 of the present paper. In brief the masses of two fragments were measured independently in coincidence by the V-E (time of flight, velocity-energy) method and their total mass in the event is determined. If it is significantly smaller than the mass of the initial system, this serves as a signature of a multibody decay. It is the so-called "missing-mass" approach.

The key problem with the "missing-mass" method consists in the continuous background of scattered primary fission fragments from binary fission, which can simulate the CCT products by mass. In order to improve the reliability for defining the CCT events we have used neutron coincidences in a new compact experimental set-up (COMETA: COrrelation Mosaic E-T Array). We have introduced additional experimental variables sensitive to the nuclear charge as discussed in ref. [1]. Further, we show in the present work that the multiplicity of the neutrons emitted in fission is also a very effective tool for the search of new and different CCT modes.

The paper is organised as follows, in sect. 2.1 we first repeat the description of the experiment reported in ref. [1], where the CCT effect has been observed. Then the details of the two new experiments with neutron coincidences are described in sect. 2.3. This section includes a discussion to the specific geometry of the neutron detector, which gives a relative increase of the efficiency for the registration of the isotropic component of neutron emission. The results of the experiments are compared first for the inclusive (ungated data) in sect. 3. The results with the neutron coincidences are reported in sect. 4, triple coincidences of fragments in Ex3 are presented in sect. 5, followed by a discussion of the results in sect. 6. Conclusions

are summarised in sect. 7. These are related mainly to the unusual type of spectrometric information, namely regular linear structures in the mass correlation distributions shown as scatter plots. Special attention is paid for demonstrating the reliability of the unique structures. We refer to both the mass resolution achieved (sect. 4.3), and to the quantitative estimation of the significance of the patterns with rare events and their non-random nature (appendix. A).

2 Experiments

We discuss here the experimental set-up of three different experiments devoted to the search for collinear cluster tri-partition of ^{252}Cf (sf). The TOF-E (time-of-flight *vs.* energy) method for the measurements of two FF masses in coincidence with two detectors placed at 180 degrees was used in all three experiments. In this method, the fragment velocities V, obtained by means of TOF and the energy E are measured for each detected fragment individually. The fragment mass M is calculated simply using the equation $M = 2E/V^2$. Only two fragments were actually detected in each fission event (in the two detectors, at 180°). Their total mass, the sum M_s will serve as a sign of a multi-body decay, if it is significantly smaller than the mass of the initial system ("missing-mass" method). Along with the "missing-mass" method, a direct detection of all three CCT partners was possible in Ex3 (see sect. 5 for details). In the two new experiments additional gating by the experimental neutron multiplicity linked with fission events has been used.

2.1 Experiment Ex1

In the first experiment (Ex1, fig. 1), performed at the FOBOS [13] set-up in the Flerov Laboratory of Nuclear Reactions (FLNR) of the Joint Institute for Nuclear Research (JINR) in Dubna, about 13×10^6 coincident binary fission events have been collected. It has the highest statistics among all three experiments discussed here. Below we repeat the description of the experiment, with labels for the components illustrated in fig. 1 from ref. [1].

The TOF of the fragment has been measured over a flight path of 50 cm between the "start" detector, label 3 in fig. 1, which is based on micro-channel plates (MCP) placed next to the ^{252}Cf source and the "stop" detectors formed by position-sensitive avalanche counters (PSAC, 4). Calibration procedures used in Ex1 and Ex2 for the gas-filled detectors are presented in ref. [14].

The source activity was 370 fissions/s, deposited on a Al_2O_3 backing of $50 \mu g/cm^2$ thickness and 18 mm in diameter —(1). Through the measurements of the position the PSACs provided also the fragment emission angle with a pre-scission of 1°. The energies of those coincident fragments, which passed through the PSACs were measured in the Bragg ionization chambers (BIC, 5). The entrance windows of the large BIC made of $1 \mu m$ thick aluminised
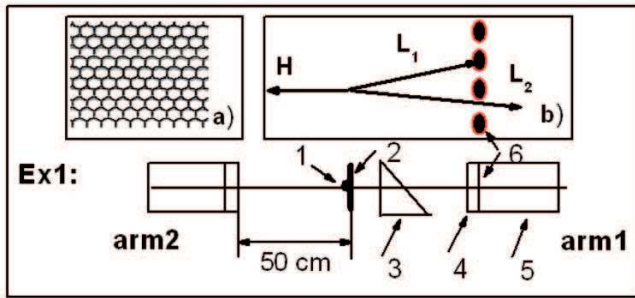
Fig. 1. Scheme of (Ex1) for coincidence measurements of two fragments of the collinear decay of ^{252}Cf. Here: 1 —Cf source, 2 —source backing, 3 —micro-channel plate (MCP) based timing "start" detector, 4 —position-sensitive avalanche counter (PSAC) as "stop" detector, 5 —ionization chamber (BIC) with the supporting mesh, 6 —mesh of the entrance window. The front view of the mesh is shown in the insert a), a mesh section is presented in the insert b). After passage of the two fragments through the source backing, two light fragments, L_1 and L_2 (originally fragment L), are obtained with a small angle divergence due to multiple scattering. One of the fragments (L_1) can be lost hitting the metal structure of the mesh, while the fragment L_2 reaches the detectors of the arm1 (insert b). The source backing (2) exists only on one side and causes an angular dispersion in the direction towards the right side (arm1).

Fig. 2. Layout of the experiment (Ex2) for the neutron coincidences with the modified spectrometer based on FOBOS detector modules (1), a "neutron belt" consisting of 140 ^{3}He-filled neutron counters (2), and a "start" avalanche counter with the Cf source inside (3).

Mylar, have a diameter of 385 mm. To withstand the pressure of the working gas, the delicate window foil has to be supported by a twofold structure —a concentric heavy carrier of a transparency of 94% and an adjacent etched Ni mesh having a cell dimension of 2.7 mm in diameter and 0.9 mm bulkhead in between the open pores. The thickness of the mesh is about 1 mm. The geometrical structure of the mesh is hexagonal, its front view is shown in the insert a) of fig. 1, a mesh section is presented in the insert b). The mesh reduces the transparency of the entrance window to 75%. This mesh is a very important peculiarity of the experiment (blocking one of the fragments), as explained in the caption to fig. 1 and in ref. [1].

2.2 Experiment Ex2

The second experiment (Ex2) discussed here has been carried out with the modified FOBOS spectrometer also at the FLNR of the JINR. The layout of the experimental set-up is shown in fig. 2. Due to the low yield of the process under study, a multi-arm configuration containing five big and one small standard FOBOS modules in each arm was used. The distance to the source is again 50 cm. Such a scheme of a double-armed TOF-E spectrometer allows the measurement of energies and velocity vectors of the coincident fragments and covers $\sim 16\%$ of the hemisphere in each arm. In order to provide "start" signals for all of the modules only wide-aperture start detectors capable to span a cone of $\sim 100°$ at the vertex could be used. Another point to be taken into account when choosing appropriate start detectors, arises from the expected decay kinematics (fig. 1, insert b). Among two fragments flying
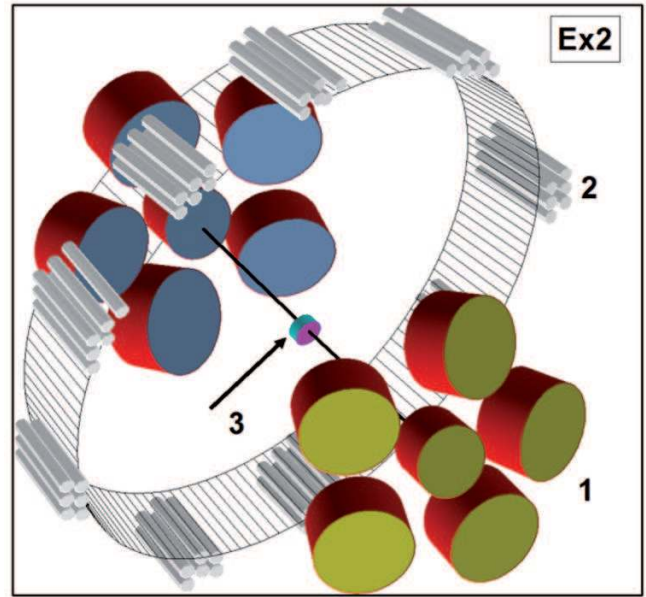
in the same direction only the faster one will be assigned a correct TOF, if the start detector is located at some distance from the decay source. Both problems are solved in the specially designed very compact three-electrode start avalanche counter, in which a central electrode (cathode) is combined with the ^{252}Cf fission source (330 fissions/s, and a Al_2O_3 backing of $50\,\mu g/cm^2$ thickness).

From the results of our previous experiments we can assume, that there are several CCT modes [15], with the middle fragment of the three-body pre-scission chain with very low velocity after scission. The existence of such modes has been confirmed by both our new results discussed here and by calculations [6]. The neutrons emitted from the moving binary fission fragments are focused predominantly [16] along the fission axis. In order to exploit this difference for revealing the CCT events, the "neutron belt" was assembled in a plane perpendicular to the symmetry axis of the spectrometer, which serves as the mean fission axis at the same time (fig. 2) [17]. The center of the belt coincides with the location of the fission source. The neutron detector consists of 140 separate hexagonal modules comprising ^{3}He-filled proportional counters, a moderator, a high-voltage input and a preamplifier. The counters operate under a gas pressure of 7 bar, being 50 cm in length and 3.2 cm in diameter. The moderator is made of polyethylene. The neutron counters cover altogether $\sim 29\%$ of the complete solid angle of 4π. The "neutron belt" consists of two layers of neutron registration modules. At the testing stage we have found that more than 90% of the neutrons were detected in the two first layers of the counters. For this reason the third layer was omitted in the final version of the set-up.
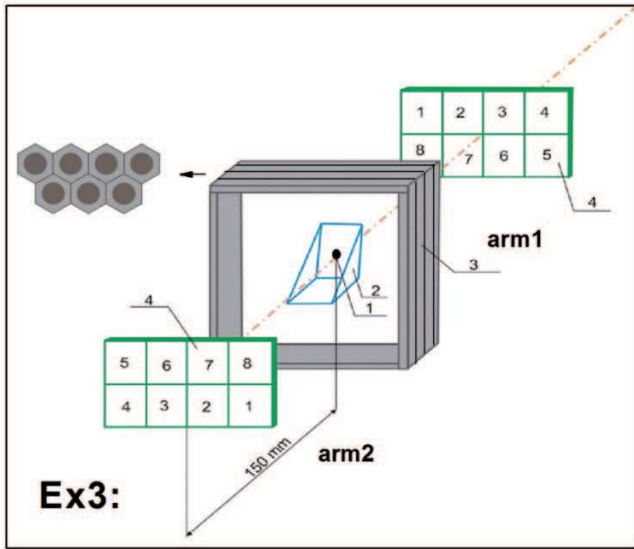
Fig. 3. Scheme of the COMETA set-up of Ex3, which consists of two mosaics of eight PIN diodes each (4), MCP-based start detector (2) with the ^{252}Cf source *inside* (1), and a "neutron belt" (3) consisting of 28 ^{3}He-filled neutron counters in a moderator. The cross-section of the belt is marked by the arrow.

The registration efficiency for neutrons does not exceed 4% for those emitted in normal binary fission and it is 12% for neutrons emitted isotropically. The electronics of the "neutron belt" is operated in slave mode being triggered by the fission event selector. All in all more than 2×10^6 fission events in coincidence with neutrons were detected.

2.3 Experiment Ex3

The experiment Ex3 has been performed as the two previous ones at the FLNR of the JINR using the COMETA set-up (fig. 3). It is a double-arm time-of-flight spectrometer which includes a micro-channel plate (MCP) based "start" detector with the ^{252}Cf source inside, similar to that used in Ex2. Two mosaics of eight PIN diodes each and a "neutron belt" comprising 28 ^{3}He-filled neutron counters are used. Each PIN diode (2×2 cm of surface area) provides both energy and timing signals. The actual active area of the PIN diodes is a little bit smaller due to the multi-aperture diaphragma, non-transparent for the FFs, covering the mosaic as a whole. The diaphragma provides demarcation strips between neighbouring diodes of ~ 3 mm width. Thus an angle between the fragments L_1 and L_2 (see fig. 1b) must be more than 1° in order to be detected in neighbouring diodes. In this way the structure provides the dead zone, where one of the fragments can get lost (similar to Ex1, fig. 1b). Each flight path is 15 cm.

The use of the Si semiconductor detectors in TOF-E spectrometry of heavy ions (or FFs) is known to have delicate methodological problems due to the "amplitude (pulse-height) defect" [18] and "plasma delay" [19] effects in the E and TOF channels, respectively. The first effect involves a non-linearity in the dependence of the

"deposited energy *vs.* electrical charge measured", while the latter distorts the TOF used in the calculation of the heavy-ion masses. We have worked out an original approach for the accounting of the amplitude defect and the correct reconstruction of the FF mass in TOF-E measurements [20]. Unfortunately it is valid only for the case when a dispersion of the plasma delay time can be ignored due to a long flight path used. This is not the case here.

To overcome the problem we have used a simplified approach as follows. Two coefficients of the linear time calibration are calculated using the velocity spectrum of the known FFs from the literature. The energy calibration dependence is presented as a parabolic curve passing via three points, namely through the known centers of the energy peaks for the light and heavy fragments, and the energy of the alpha-particles of the natural radioactivity of ^{252}Cf nucleus. Such approach gives quite satisfactory results for the reconstruction of the FF masses, at least, in the vicinity of the *loci* of binary FFs, as shown below.

The neutron belt is located in the plane perpendicular to the symmetry axis of the set-up. According to modelling and previous experiments, the detection efficiency is estimated to be $\sim 5\%$ and $\sim 12\%$ for the neutrons emitted in binary fission and from an isotropic source, respectively [21]. The total statistics of binary fission events collected for Ex3 in coincidence with neutrons is about 4×10^6 events.

2.4 Efficiency for the registration of CCT events

The registration of the CCT events is based on a double time-of-flight–energy (TOF-E) measurements and a particular geometrical blocking effect, already introduced in refs. [1,15] and is shown in fig. 1. In this section we give a discussion of the geometrical differences of the three experiments. These are partially contained in the description of each experiment. We summarise that the missing-mass approach is linked to the blocking of parts of the solid angle of the E-detectors and the dispersive effect of the backing of the source. For the two collinear (relative angle 180°) fragments, which come from the first neck rupture, as in binary fission, one is reaching the energy detectors undisturbed ($A1$). For the second neck rupture of the other fragment ($A23$), again two fragments ($A2$ and $A3$) are produced collinearly, however, these are dispersed in the backing of the source and in other media (start detectors), into a fork with a certain opening angle. In Ex1 and Ex2 the support grid of the gas-ionisation chambers act as blocking medium over the whole area of the solid angle of the ionisation chambers. In Ex3 these are the narrow regions around the frames defining the solid angle of the E-detectors (PIN diodes), see fig. 4. A fork of two fragments, hitting the mosaic detectors can give rise to three different types of events.

- Blocking can occur if the opening angle of the fork lies in the range $0° < \theta < 1°$ (missing-mass event marked as 1-2-3 in fig. 4). As a consequence only an area along the border lines of the PIN diodes is available to register CCT events with a missing mass. The opening
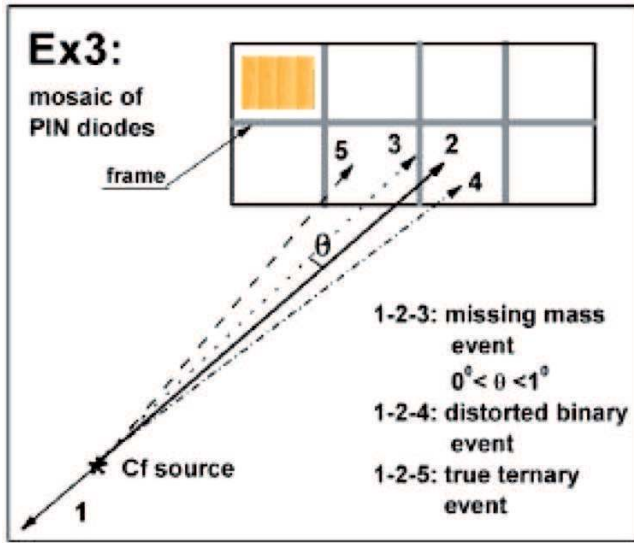
Fig. 4. The geometry in Ex3 with the PIN diodes. Hitting the mosaic by a fork of fragments can give rise to three different types of events. Blocking can occur if the opening angle of the fork lies in the range $0° < \theta < 1°$ (missing-mass event marked as 1-2-3). Both fragments of the fork can hit the same PIN diode (event 1-2-4). If $\theta > 1°$ the fragments forming the fork can be detected in two different PIN diodes (true ternary event 1-2-5).

angle of the fork θ is expected to be around $1°$ [1]. In the actual geometry of Ex3 approximately 60% of the whole area is active for the blocking of one of the fragments in the fork.

– Both fragments of the fork can hit the same PIN diode (event 1-2-4 in fig. 4). In this case the masses of the fragments are not correctly determined. An interesting manifestation of such events will be discussed below in sect. 5.

– If $\theta > 1°$ the fragments forming the fork can be detected in two different PIN diodes (true ternary event 1-2-5 in fig. 4).

In order to define the differences in the structures of the M_1-M_2 plots, we can use an expression which defines the experimentally observed yield $Y_{exp-CCT}$ of a distinct CCT mode. It can be estimated as follows:

$$Y_{exp-CCT} \sim Y_{phys} \times P_{miss}. \tag{1}$$

Here Y_{phys} is the relative (per binary fission) physical yield of the corresponding collinear ternary decay mode, P_{miss} is the probability that one of the CCT partners will be lost while two others are detected, defining the missing-mass approach.

Further for neutrons in coincidence (in Ex2 and Ex3), P_n defines the probability to register n neutrons in coincidence with the FFs from the CCT decay. For this case, eq. (1) must be amended as follows:

$$Y_{exp-CCT}^n \sim Y_{phys} \times P_{miss} \times P_n. \tag{2}$$

For Ex1 the opening angle of the fork must be larger than $0.15°$ in order that one of the fragments gets blocked.

For Ex2 this angle is very similar, or slightly larger, the blocking structure is homogenously distributed over the whole solid angle. For Ex3 this condition is quite different, the blocking medium is determined mainly by the spaces between two PIN diodes, which is given by the frames. The efficiency to register a blocking event is a factor 3 smaller.

3 Inclusive data for experiments Ex1, 2, 3

The analysis is based on the presentation and discussion of two-dimensional diagrams of the registered masses (M_1 and M_2), in which the sum M_s of the two masses can be discussed. The events with total masses $M_s = M_1 + M_2$ will appear as diagonal lines in the mass correlation plot. Projections onto an axis showing either M_1 or M_2, are also used. Several cases where in the two-dimensional plot horizontal lines can be identified, which are due to the formation of specific masses, $M_{1,2} = $ const, in combination with complementary partners of varying mass. These are well seen for higher neutron multiplicities in the neutron gated data (sect. 4).

3.1 Experiment Ex1

We repeat shortly the results reported in ref. [1]. The most pronounced manifestation of the CCT as a missing-mass event is a bump (fig. 5a) in the two-dimensional mass-mass correlation plot. In this distribution of the fission fragment masses, the bump occurs only in one of the spectrometer arms with dispersive media (M_1), whereas it is absent in the analogues variable for the second arm (M_2). The bump is marked by the arrow in fig. 5a. We see two great bumps due to binary fission, the pronounced vertical and horizontal intensities are due to binary fission fragments scattered from the entrance support grid for the windows of the gas detectors (see fig. 1). Actually this background becomes negligible in Ex3.

3.2 Experiment Ex2

The inclusive results as obtained in the experiment Ex2 (fig. 2) (with lower statistics) confirm the results of Ex1. New aspects are obtained by gating the FF mass-mass distributions on the number of neutrons detected in coincidence (sect. 5), see also ref. [22].

At first we will compare the results of Ex2 without neutron gating, with those obtained in Ex1. The FF mass correlation plot, similar to that obtained in Ex1 (fig. 5a) is shown in fig. 6a. Projections of this distribution both on the M_1 axis and on the $M_s = $ const directions are presented in figs. 6b, and c, respectively. They are compared with the analogous spectra from the experiments Ex1, including the result from the $^{235}U(n_{th}, f)$ reaction [1].

The bump in the projected FF mass correlation data in fig. 6b is centered around magic isotopes of Ni, these are
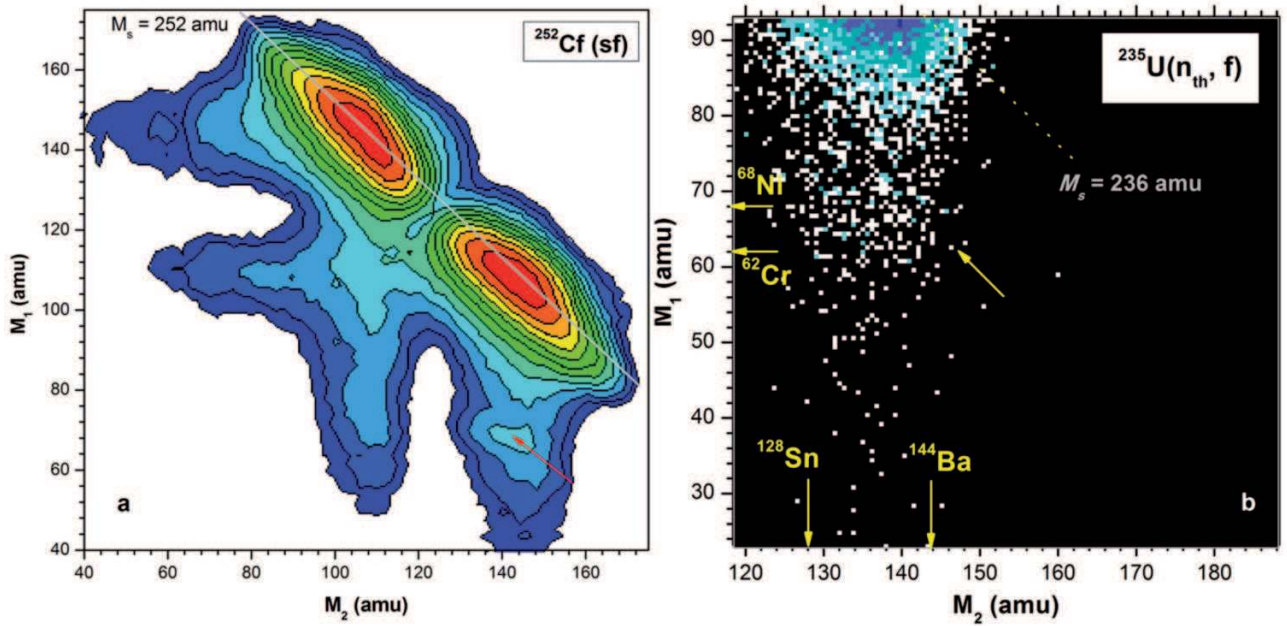
Fig. 5. a) Ex1 (Color online). Contour map (in logarithmic scale, the steps between the lines are approximately a factor 2.5) of the mass-mass distribution in Ex1 of the collinear fragments of ^{252}Cf (sf), detected in coincidence in the two opposite arms of the FOBOS spectrometer. The specific bump in the yields in arm1 is indicated by an arrow. b) The region "around the bump" in the mass-mass distribution for the FFs from the reaction ^{235}U(n_{th}, f) from ref. [1]. The bump is bounded by magic numbers of clusters (marked by corresponding symbols near the axes). The tilted arrow shows a valley between the ridges $M_s = M_1 + M_2 = \text{const} = 208\,\text{amu}$ and $M_s = 212\,\text{amu}$.

the isotopes of ^{68}Ni, ^{70}Ni and ^{72}Ni having magic number of protons $Z = 28$. The first one can be called a "one and half" magic nucleus due to the neutron sub-shell $N = 40$ [23,24], while the last one has nucleon composition corresponding to the unchanged charge density hypotheses (Z_{ucd} hypotheses) [25,26]. The middle isotope of ^{70}Ni showing enhanced yield in far asymmetric fission [23] is likely a compromised version in between two already considered nuclei. This bump will be called below as the "Ni" bump. The bump marked by the arrow in fig. 6a looks less pronounced as compared to that obtained in Ex1 (fig. 5a). This can be partially explained by a worse mass resolution due to a larger total thickness of the foils along the flight pass (see sect. 4.3 for details). Projections for Ex2 are shown in the "difference" version, *i.e.* as a difference of the tail regions in arm1 and in arm2, respectively. The second peak at lower masses in Ex2 looks more pronounced, it corresponds to the complicated two-dimensional structure centered at $M_1 \sim 56\,\text{amu}$ in fig. 10. Overall a good agreement is observed in the position of the peaks in figs. 6b and c for all three experiments. The shift of the peak for the ^{235}U(n_{th}, f) reaction in fig. 6c has already been discussed in ref. [1].

3.3 Experiment Ex3

This methodically quite different experiment confirms our previous observations concerning the structures in the missing-mass distributions. In this case there is no tail

due to scattering from material in front of the E-detectors. Figure 7a shows the region of the mass distribution for the FFs from ^{252}Cf (sf) around the "Ni" bump ($M_1 = 68$–$80\,\text{amu}$, $M_2 = 128$–$150\,\text{amu}$). The structures are seen in the spectrometer arm facing the source backing only. No additional selection of the fission events has been applied in this case, the experiment has no background. A rectangular-like structure below the locus of binary fission is bounded by magic nuclei (their masses are marked by the numbered arrows) namely ^{128}Sn (1), ^{68}Ni (2), ^{72}Ni (3). In fig. 7b we show the projection of the linear structure seen at the masses 68 and 72 amu. Peaks seen in fig. 7b allow to estimate a mass resolution of the COMETA set-up to be $< 2.0\,\text{amu}$ (fwhm).

Two tilted diagonal lines with $M_s = 196\,\text{amu}$ and $M_s = 202\,\text{amu}$ (marked by number 4) start from the partitions 68/128 and 68/134, respectively. In experiment Ex1 [1], fig. 6, similar sub-structures have been seen for masses $M_s = 204, 208, 212, 214\,\text{amu}$, where they were revealed indirectly —by applying a method of the second derivative filter, in an absolutely statistically reliable distribution. We emphasize the difference in the geometry of the blocking mediums in Ex1 and Ex3, which are decisive for the relative experimental yields of the CCT modes with different angular distributions between the fragments forming the fork (see sect. 2.4). We observe the preference of lighter mass partitions which produces the tilted ridges in Ex3. The positions of the points in the lower part of fig. 7a confirm the possible existence of the ridges revealed in Ex1, with the following magic partitions assigned to
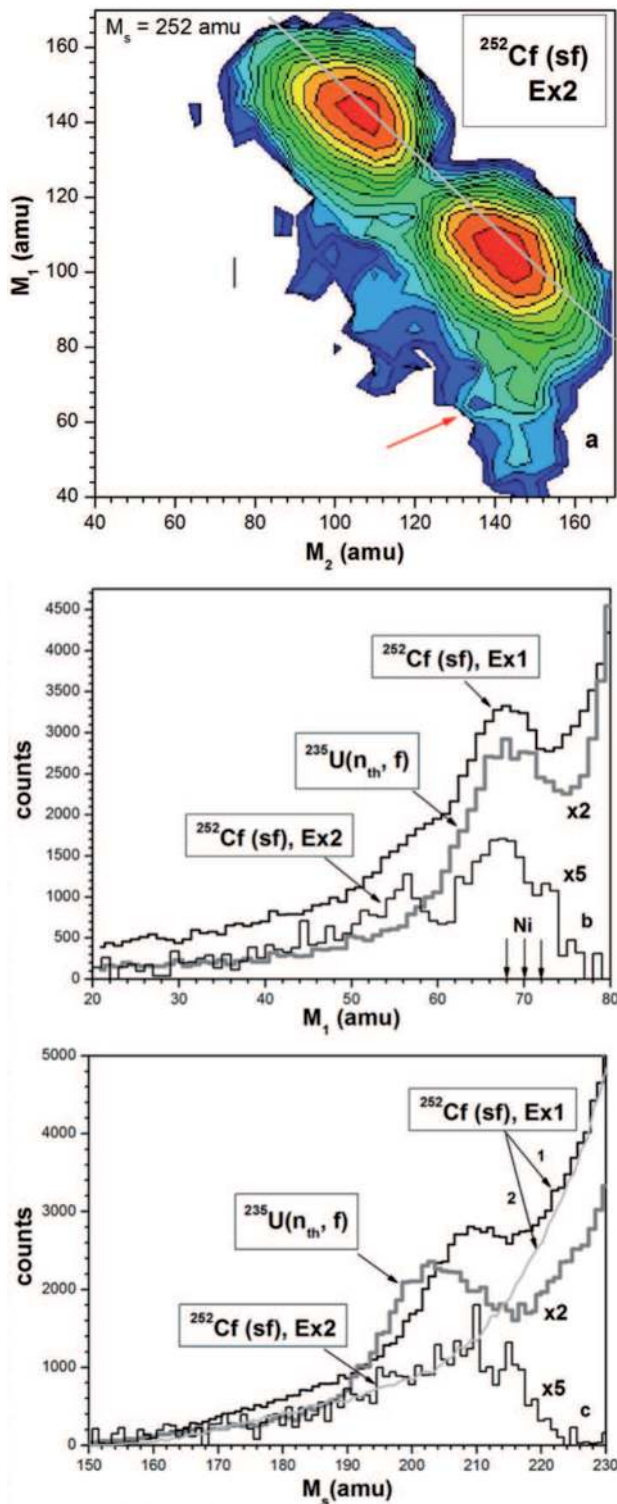
Fig. 6. (Color online) Ex2: a) Contour map of the mass-mass distribution (logarithmic scale, with lines approximately a step factor of 1.5) from a coincidence in the two opposite arms of Ex2. The bump in the spectrometer arm (arm1) facing the backing of the Cf source is marked by the arrow. b) Projections onto the M_1-axis for comparison with the experiment Ex1, and with the results of the ^{235}U(n_{th}, f) reaction [1]. Positions of the magic isotopes of Ni are marked by the arrows (see text of sect. 4.2 for details). c) Projections onto the direction $M_s = M_2 + M_1$. The result for Ex1 is presented by two curves marked by the arrows 1 and 2 (dotted) for the arm1 and arm2, respectively. For Ex2 the yield of arm2 is subtracted
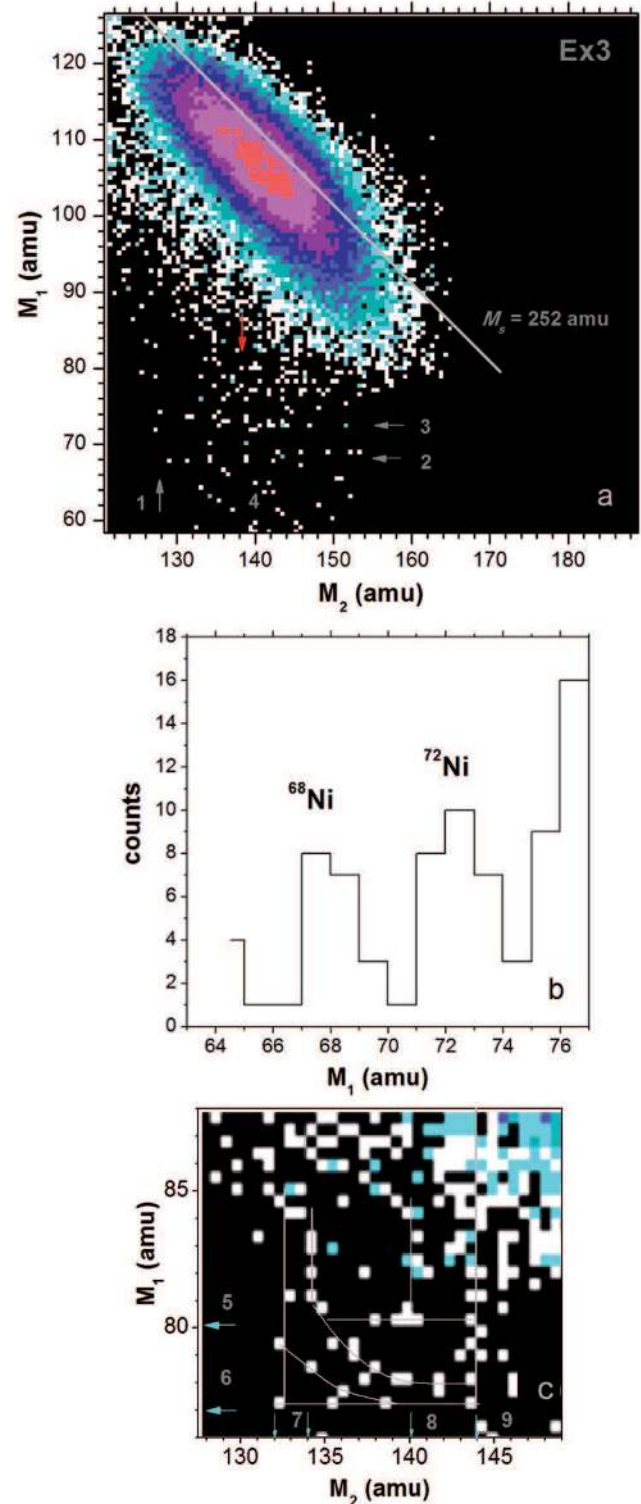
Fig. 7. (Color online) Results of Ex3: The region of the mass-mass distribution for the FFs from ^{252}Cf (sf) around the CCT bump (figs. 5a and 6a). No additional gates were applied (there is no background of scattered fragments) due to the use of PIN diodes. An internal structure of the "bump" seen as the horizontal lines (marked by the arrows, 2 and 3 is shown in fig. 7b) as a projection. A part of the plot just below the *locus* of binary FFs produces the rectangular structure (marked by the red arrow in part a), already seen before, it is shown in a larger scale in fig. 7c). The lines are drawn to guide the eye.

the starting point of the ridges: 70/134 ($M_s = 204$ amu), 68/140 ($M_s = 208$ amu), 68/144 ($M_s = 212$ amu), 70/144 ($M_s = 214$ amu).

Thus, the comparison of Ex1 and Ex3, which are very different both by the structure of the detectors and the mass calculation procedures used, as well as the statistics collected, still gives a strong confirmation of the existence of tilted ridges $M_s = $ const linked with magic partitions. As can be inferred from fig. 7a, the yield of the FFs with the mass 128 amu, which is extremely low in conventional binary fission, is clearly seen, scattered binary fragments cannot give rise to this structure. A part of the plot just below the locus of the binary FFs for a little bit lower statistics is shown in a larger scale in fig. 7c. The structure is bounded by the magic nuclei of ^{80}Ge, ^{77}Zn, ^{132}Sn, ^{144}Ba (their masses are marked by the arrows 5, 6, 7, 8, respectively). According to the shell correction map from [27] the nucleon composition of the ^{77}Zn isotope corresponds to a deformed shell for both neutrons and protons. The stabilizing effect for mass numbers around $A = 76$ in conventional ternary fission is reported in ref. [28]. The structures observed in fig. 7 agree in most aspects with the rectangular structures seen in the neutron gated data of Ex2.

These observations point to the fact that the CCT decay occurs in a large variety of modes (mass combinations), which could not be distinguished in Ex1 without additional gating due to the large background from scattered FFs.

Likely due to the difference in the parameters of the blocking mediums, the experimental yield of the "Ni" bump in Ex3 does not exceed 10^{-3} per binary fission, *i.e.* it is much less then in Ex1 and Ex2. At the same time with the absence of scattered FFs in Ex3, we were able to observe the internal structure, without any additional cleaning of the FF mass distribution.

4 Results of neutron gated data for the experiments Ex2 and Ex3

The spectrum of the measured neutron multiplicities is presented in fig. 8. For comparison, a similar spectrum, but measured in a 4π geometry and calculated for an efficiency of 100% with corrections from ref. [22], is shown in the insert a) of this figure. Actually the experimental neutron multiplicity spectrum in our experiments is formed as a superposition of several components. Each partial neutron multiplicity (panel a) is transformed according to the binomial law and contributes to the experimental neutron multiplicity spectrum. During the time gate used to trigger by a fission event for reading the neutron counters, neutrons from previous fission events as well as neutrons from the background of the experimental hall can give additional contributions to the number of neutrons detected during the time gate opened by a fission event. These two sources have been calculated in the frame of the model for the neutron registration channel [17] and are shown in fig. 8 (the curves marked as "pile-up" and "background").
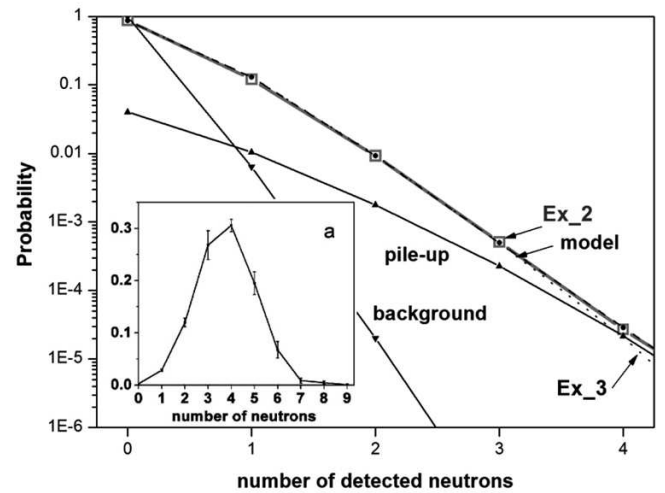

Fig. 8. Neutron multiplicities measured in Ex2 (gray rectangles) and Ex3 (dotted line) in coincidence with fission fragments. The error bars do not exceed the dimension of the symbol. Calculated multiplicities for Ex2 are shown by a dashed line (marked as "model"). Contributions of the background and pile-up events in Ex2 are marked as "background" and "pile-up", respectively. Panel —insert a) depicts the spectrum of neutron multiplicities for ^{252}Cf (sf) from ref. [22] measured in 4π geometry and recalculated to a registration efficiency of 100%.

The model with the parameters known from both, the experiment [29] and from those estimated using the MCNP code [30], reproduces the experimental data very well.

It should be stressed that experimental neutron multiplicities in our work are used for gating of coincident fission fragments only. Reconstruction of the absolute neutron yields, similar to those shown in the insert of fig. 9 is quite a different task beyond the scope of this work.

4.1 Experiment Ex2

As mentioned before in sect. 2.2, the experiment under discussion with coincident neutrons was motivated by the expectation that the center fragment is connected to an isotropic neutron source of increased (as compared to binary fission) multiplicity linked with the CCT. For this reason a selection of the fission events with an increased number of detected neutrons was studied. Due to restricted statistics collected, we start with the gate set to $n = 3$, where n is the number of detected neutrons.

The corresponding mass distribution is shown in figs. 9a and b. A rectangular structure is marked by the arrow. It is observed in the same arm as the bump in figs. 5a, 6a. The events forming the rectangle and its vicinity lie in the box $w1$ in the V_1-E_1 distribution presented in the insert. Additional selection with this $w1$ gate reveals the rectangular structure in a more pronounced way (fig. 9b). The rectangle lies well below the line with $M_s = M_1 + M_2 = 252$ amu and it is bounded by the magic isotopes of ^{94}Kr, $^{80-82}$Ge, ^{128,132}Sn, and ^{144}Ba,
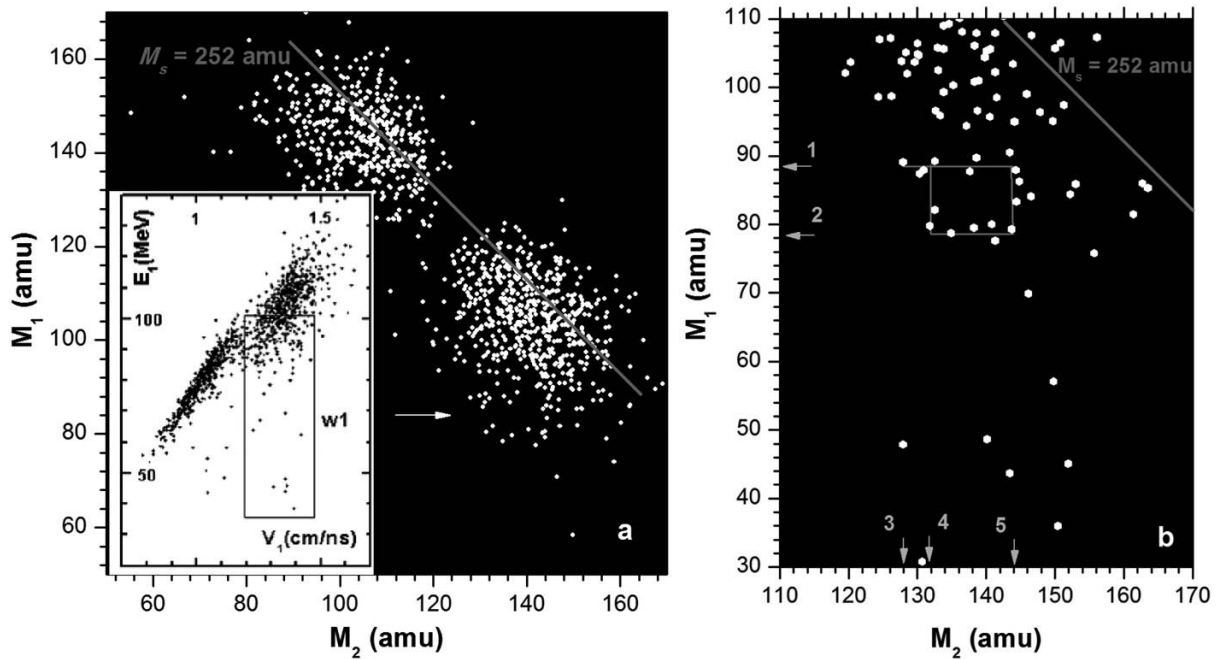
Fig. 9. Results of Ex2 ($n = 3$): a) Mass-mass distribution of the FFs for the multiplicity ($n = 3$). A rectangular structure is marked by the arrow. b) Mass-mass plot for the events in Ex2 with ($n = 3$) and a gate $w1$ in the V_1-E_1 plot shown in the insert. The rectangular structure in the plot is bounded by the magic numbers in nuclei with the masses (M_2: 132–144 amu) and (M_1: 78–88 amu), these are marked by the arrows. The lines are drawn to guide the eye. See text for additional details.

their masses are marked by the arrows are 1–5, respectively.

Using a similar procedure for $n = 2$, more events remain and complicated structures appear (fig. 10). A larger concentration of events in the plot appear within boundaries of masses as marked in the figure (magic isotopes of ^{94}Kr, ^{128}Sn, ^{68}Ni). The extension of the points in the right half of the rectangle, likely reflects shell effects around $N = 88$ (neutrons) in the shell correction map [31].

There is negligible background from scattered binary fission fragments in these data, we emphasize the non-random nature of the whole plot. The "tail" of scattered fragments should look like a smooth curve decreasing monotonically from the *locus* of conventional binary fission (see, for instance, curve 2 in fig. 6c). This is not observed here. The most populated rectangular structure is bounded by magic nuclei, as was mentioned before. The bulk of the points below this structure lie, within mass resolution, only along four discreet directions, namely M_1 or $M_2 = $ const, $M_1 + M_2 = M_s = $ const (it means that the missing mass is const) and the line to be almost perpendicular to it. In order to have an idea of such different structures these possible directions are shown in the lower right corner of the plot for visual comparison with the data. One of the examples of the lines with $M_s = $ const is marked by the number 7, this line corresponds to a missing ^{14}C nucleus.

In order to estimate quantitatively a probability of a random realisation of the lines under discussion, special Monte Carlo testing was performed using a well-known formalism of the Hough transformation [32,33] for formal
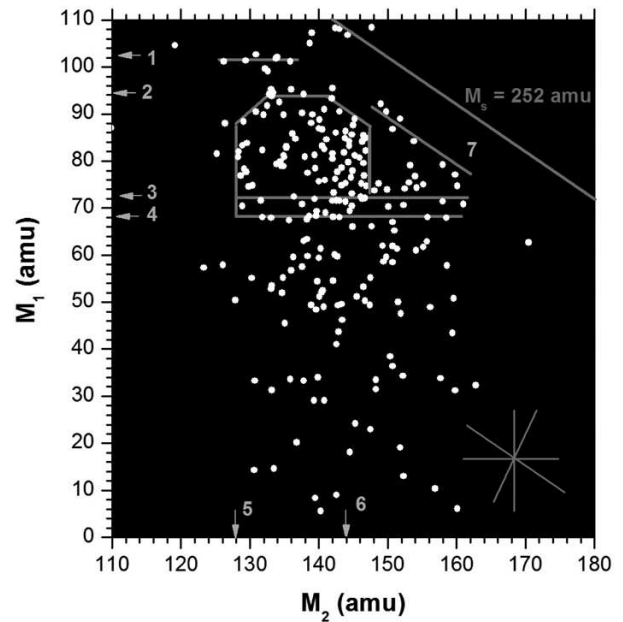

Fig. 10. Ex2: results for neutron multiplicity, $n = 2$, the mass-mass distribution of the FFs, and a additional gate $w1$ as in fig. 9a in the V_1-E_1 plot. This diagram contains no background from scattered particles. Arrows with numbers 1–6 mark the positions of masses of magic nuclei, a line numbered 7 points to events with the loss of a ^{14}C nucleus, as discussed below. The main intensity is with masses for the third fragments from 36–20. The lines are drawn to guide the eye. See text for more details.
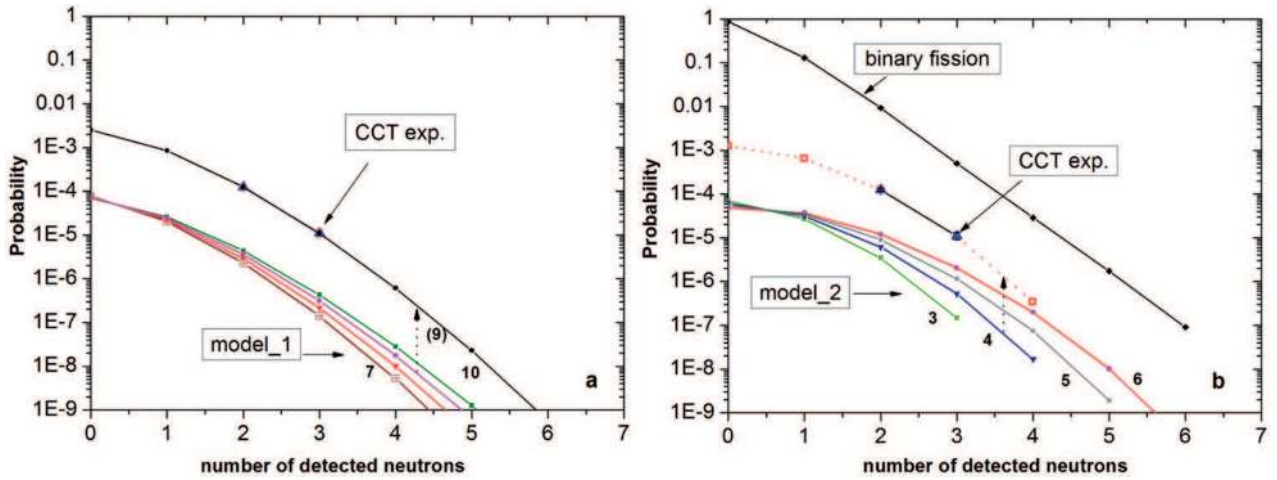
Fig. 11. (Color online) a) Comparison of the neutron yields associated with CCT (error bars do not exceed the dimension of the symbol) and spectra for neutrons emitted from the accelerated fission fragments (model_1), and b) isotropic neutron sources (model_2) of different multiplicities (marked near curves). Each curve is normalised arbitrary to the total yield 10^{-4}. The model curves, which provide the best agreement of the slopes with those of the experimental observations are marked by the arrows. See text for details.

revealing of lines consisting of several points. The probability of a random realization of such line does not exceed 2% (see the appendix for the details) and it is even much lower for a more complicated structure like the rectangle in fig. 9b.

We emphasize once more that the structures visible in figs. 9 and 10 are seen in the same spectrometer arm (and only there) as the bump shown in fig. 6. The rectangular structures have been revealed thanks to neutron gating, which effectively suppressed the background from the scattered FFs of binary fission in the region of interest, and selects different CCT modes. Each event is a true triple coincidence with E-TOF-neutrons, the neutron number is potentially much larger then 3, because of the lower efficiency for neutron detection.

4.1.1 Estimation of the CCT events as a neutron source

In our gated distributions the background due to scattered FFs is negligible, therefore a random generation of linear structures has a low probability. This is important for the interpretation of the structures seen in figs. 9 and 10. The structures are coincidences of true physical events, and must be associated with ternary fission events with at least one missing fragment. The fact that the structures appear only with neutron gating means that the neutron source, which produces these events (structures) has parameters, which differ from those of a neutron emission in conventional binary fission.

We try to estimate roughly the neutron multiplicity of the decays for the events shown in fig. 10. Among these 230 events (1.1×10^{-4} per binary fission) in coincidence with two neutrons were detected, and 17 events (8.0×10^{-6} per binary fission) in the same region of the mass correlation plot have an experimental neutron multiplicity three ($n = 3$). We can propose ternary decay modes to be connected with all the experimental points in fig. 10. The

experimental yields for the events $n = 2$ and $n = 3$ are shown in fig. 11 by the triangles.

For further discussion we suppose (model_1): that neutrons are emitted from accelerated fragments moving with the velocities typical for normal binary fission. The calculations are based on the model of the neutron registration channel presented earlier in ref. [21]. Using the slope of the experimental curve as a criterion one can try to choose the best result among the model spectra. We obtain a primary neutron multiplicity of M-$n = 9$. Very elongated pre-scission shapes are needed in order to provide such increased neutron multiplicity [22]. At the same time we observe the velocities of the detected fragments close to corresponding mean values in normal binary fission. In order to overcome the contradiction the neutron source searched for was supposed to be at rest or isotropic (model_2). The results of modelling the multiplicities of such a situation are compared with the experimental data in fig. 11b. The best agreement is observed for the slope of the curve corresponding to four neutrons emitted from the experimental center ($n = 4$).

The results of estimations of the neutron multiplicity obtained in the two different models can be judged as follows: one (model_1) failed to reproduce the experimental data, but it does not exclude that a superposition of two sources (models) exists. It is important that at least a certain part of the detected neutron multiplicity is due to a neutron source different from those originating from accelerated fragments. In refs. [34,35] and others, an isotropic component is observed in addition to the neutrons emitted from the accelerated fragments. In our case, the latter will be detected with a factor 3 lower efficiency.

4.2 Results of experiment Ex3

The FFs mass-mass distribution for the events selected with gates and the similar approach as used in Ex2, is
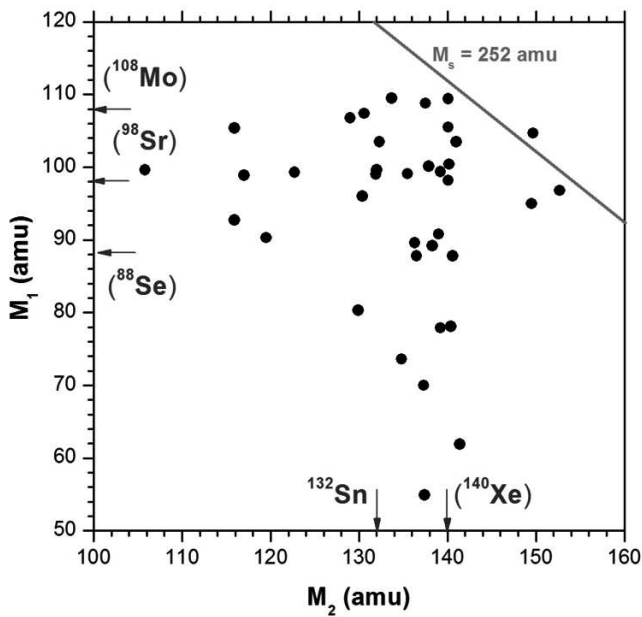
Fig. 12. Ex3 ($n = 3$, and $w1$). Results obtained at the COMETA set-up: mass-mass distribution of the FFs from ^{252}Cf (sf) under the condition that three neutrons ($n = 3$) were detected in coincidence and an additional selection with the gate $w1$, in the (V_1-E_1) distribution similar to that shown in fig. 9a of Ex2.

shown in fig. 12. Namely we chose $n = 3$ and a selection with the gate in the V_1-E_1 distribution similar to the box $w1$ in fig. 9a was applied. Again a rectangular structure similar to that seen in Ex2 (figs. 9 and 10) however, for a different mass range.

This structure is invisible in the initial ungated distribution, because it is located very close to the center of the conventional binary fission events, as can be seen from the comparison of fig. 7 with fig. 12. The additional gates help to reveal new CCT decay modes, with very light fragments ($M_3 = 22$ amu reaching down to binary fission).

As can be inferred from the figure, the rectangular structure seen in its upper right corner is bounded by the nuclei with the masses in the vicinity of known magic nuclei (shown in the brackets). These masses (except of double magic ^{132}Sn) were calculated based on the unchanged charge density hypothesis for the fission of the ^{252}Cf nucleus. Actually we know that at least three neutrons were emitted in each fission event presented in the figure. A change in the nuclear composition of the mother system can lead to a shift of the masses of the magic nuclei if neutrons were emitted from the decaying system (pre-scission neutrons). Likely, this is what we observe here. For the upper right corner of the rectangle both mass and charge conservation laws are met only if the upper side of the rectangle corresponds to $^{109}_{43}$Tc nucleus while mass 140 amu corresponds to the isotope combination of $^{140}_{55}$Cs.

The structure manifests itself exclusively thanks to the difference of the neutron sources for the fragments appearing in both binary fission and CCT, respectively. These two decay modes must differ in the neutron multiplicity

or/and in their angular distributions of the emitted neutrons in order to provide the higher registration efficiency for neutrons linked with the CCT channel. At the same time the excitation energy of the system at the scission point defined as $Eex = Q - TKE$ (where Q is the reaction energy and TKE is the total kinetic energy of all the decay fragments), is known from our experimental data. It does not exceed $Eex = 30$ MeV. This value of the excitation energy is high enough to allow for the emission of three or four neutrons, which corresponds almost to the mean neutron multiplicity of binary fission. Thus the neutron source linked with the new CCT channels must have a much smaller velocity as compared to conventional binary fragments, or it can be almost at rest in the extreme case [6]. The latter agrees with the hypothesis put forward above that we deal with the pre-scission neutrons at least for very light missing masses.

4.3 Mass resolution of the set-ups used

Experiments Ex1 and Ex2 were performed using gas-filled detectors while PIN diodes were used in Ex3. The mass resolutions achieved in each experiment are discussed separately.

4.3.1 Mass resolution in Ex2

The time-of-flight spectrum of an ^{226}Ra α-source measured at the FOBOS set-up shows a time resolution of 200 ps (irradiating a small central part of the PSAC) and ~ 400 ps if all the surface of the counter is irradiated [13] (fig. 4). Thus in Ex2 the relative time resolution does not exceed 1%.

For the energy (E), only the residual energy is measured in the BIC of the FOBOS set-up due to the energy losses in the Mylar foils along the flight pass with the total depth of about 1 mg/cm^2. The mass reconstruction procedure was presented in ref. [14]. The SRIM code [36] allows to calculate the mean residual energy and its variance for the FF after passing of all foils. The relative uncertainty (fwhm) of the measured residual energy does not exceed 2% and 3% for typical light and heavy fragments, respectively. Thus the corresponding mass resolutions (within uncertainty of time of flight) are estimated to be approximately 3 amu for light, and 4.5 amu for heavier fragments.

At the same time the *loci* of binary fission events (fig. 6a) show a much worse mass resolution (~ 6 amu and ~ 8 amu for the typical light and heavy fragments, respectively) even after "cleaning" by gating within condition $P_1 \approx P_2$, where $P_{1;2}$ are the FFs momenta (momentum conservation law). Such selection allows to exclude the events connected both with random coincidence FF-alpha-particle and scattered FFs. The estimation of mass resolution given before (3 amu and 4.5 amu) is related to an ion of a single mass, and a fixed nuclear charge, while actually in the conventional binary fission we deal with the registration of isobaric chains including normally four or five isotopes [37]. At a fixed mass number A the shape of

the fractional independent yield $Y(z)$ being non-Gaussian, differs substantially for different FF energies (table 3 in ref. [37]). Modeling using the SRIM code shows that the centers of the residual energy spectra for the adjacent isotopes of an isobaric chain are shifted relative to each other by the distance similar or even larger (for heavy fragments) then their width (for instance, $\sim 1\,\text{MeV}$ for $A = 110\,\text{amu}$ at the initial energy of $E = 112\,\text{MeV}$). Such a shift is a decisive factor for a dramatic increase of the total width of the residual energy spectrum for FFs of fixed mass after passing thick ($\sim 1\,\text{mg/cm}^2$) Mylar absorber.

It is known, as well, that some of the FFs differ essentially by the range and specific energy losses from both the calculated data and the experiments with corresponding unexcited nuclei. A mean value of $q = 3$ charge units was found [38] for the shifted part of the ionic charge state distribution thanks to an Auger cascade linked with the de-excitation of low-energy rotational levels.

The procedure of mass reconstruction briefly looks as follows [14]. Let us assume E_{ch} and V_{in} to be the energy of the fragment deposited in the BIC, respectively, its actual velocity before the BIC entrance. Both are measured in the experiment. The energy E_{cal} of the fragment after crossing of the entrance window of the BIC is calculated applying the table of energy losses [39] for the sequence of masses M_j (in the range 0–250 amu) with the nuclear charge Z_{ucd}, assigned to the corresponding fragment at fixed velocity V_{in}. In order to restore the fragment mass we examine mass by mass descending along the calculated dependence on E_{cal} (M, Z_{ucd}, at $V_{in} = \text{const}$) until the following condition is met for the first time: $E_{ch} < E_{cal}(M, V_{in})$. Strictly speaking, such procedure is absolutely correct (within energy and velocity resolution) for the fragment having really $Z = Z_{ucd}$ and which does not emit neutrons. The uncertainty due to the neutron emission would shift the calculated charge by some percents only. The uncertainty in the nuclear charge increases the dispersion and distorts the shape of the response function but its most probable value stays unbiased as it was shown in fig. 3 of ref. [1].

For Ex2 the direct the estimation gives a width of fwhm $\sim 3.5\,\text{amu}$ at the FF masses of 103 amu (line number 1 in fig. 10). A similar resolution is obtained for $M_1 \sim 94\,\text{amu}$ (the upper side of the rectangle in fig. 9b). The value obtained (3.5 amu) is very close to that cited before (3 amu) for typical light binary FFs with fixed nuclear charge. It is reasonable to suppose that the better mass resolution observed, just for the CCT partners as compared to conventional binary fragments, is due to an absence of both factors leading to the mass spread mentioned above, namely dispersion on nuclear charge at fixed mass and an increased dispersion of the ionic charge due to internal conversion.

From the neutron gated data presented here (see sect. 7) we draw the conclusion that the heavy CCT partners detected are borne rather cold and likely without angular momenta. Some of them have magic nucleon composition providing increased stiffness and stability [31].

4.3.2 Mass resolution in Ex1

In Ex1 MCP-based "start" detectors and thinner foils in the gas-filled detectors (total thickness of all the foils along the flight path does not exceed $0.6\,\text{mg/cm}^2$) allow a better mass resolution in Ex1 as compared to that in Ex2. For the conventional binary fission events, selected within the condition on the momenta $P_1 \approx P_2$, the mass resolutions are estimated to be 4 amu and 6 amu for the typical light and heavy fragments, respectively.

4.3.3 Mass resolution in Ex3

The time resolution obtained with alpha-particles at the COMETA set-up is better than 330 ps [40]. The mean velocity of the Ni-nuclei linked with the lines 2, 3 in fig. 7a observed in Ex3 is about 0.75 cm/ns, this gives a relative time resolution of about 2.7%.

The energy resolution of the semiconductor Si detectors is mainly defined by the fluctuations of the pulse height defect (PHD). For instance in ref. [41], the energy resolution of the PIN diode did not exceeded 1.7 MeV for ^{127}I ions at the beam energy of 80 MeV. Assuming the energy resolution to be inversely proportional to the PHD value, we can roughly estimate (fig. 6 in ref. [41]) for our case a value of 0.25 MeV. Thus the estimated mass resolution does not exceed 2.5 amu. This value agrees well with our data. In fig. 8 we show the projection of the linear structure seen in at the masses 68 and 72 amu. Peaks seen in fig. 8, which follow $M_1 = 68\,\text{amu}$ and other structures in fig. 7, correspond to a mass resolution of the COMETA set-up to be $\sim 2.0\,\text{amu}$ (fwhm).

Due to the rather short flight pass used in the COMETA set-up, the mass resolution is determined mainly by the relative time resolution. For the typical light fragment from binary fission, which is faster and heavier, than a Ni fragment from the CCT process, the mass resolution is calculated to be $\sim 6\,\text{amu}$. It is very close to the estimation obtained from the width of the main locus of fission fragments in fig. 7a.

5 Triple coincidences in Ex3

Another opportunity, namely the observation of slow fragments from the ternary decay as almost isotropic neutron source is confirmed by other results of Ex3. The individual detectors of the mosaic in the COMETA set-up allow in principle a triple coincidence, the direct detection of all three partners of a ternary decay. For the sake of convenience, the FFs from such events are labelled as m_1, m_2 and m_3 in an order of decreasing masses in the ternary event. Thus designations M_1, M_2 for this case m_1, m_2 are different from their previous use. For this case, we plot the m_1-m_2 correlation obtained in Ex3, in fig. 13. The rectangular structures in the center of the figure are bounded by the same isotopes (^{108}Mo, $^{128,132}\text{Sn}$, ^{140}Xe) or similar (^{110}Tc, ^{102}Zr) magic clusters (their masses are
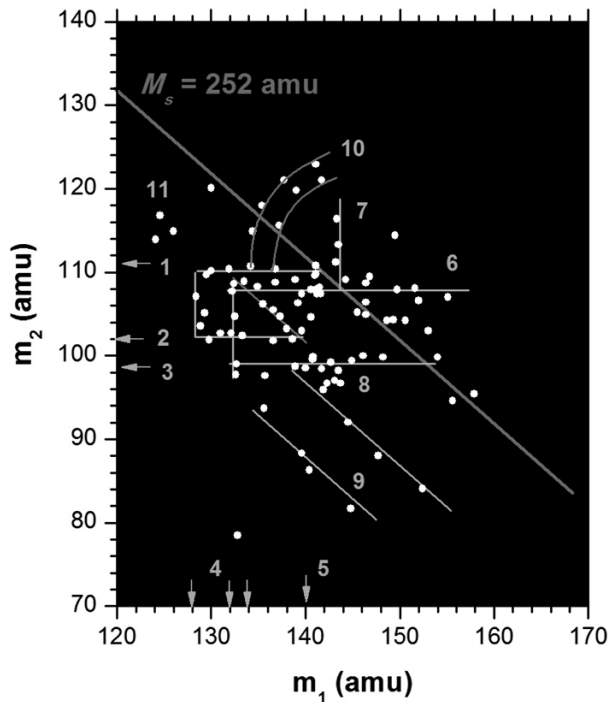
Fig. 13. Ex3, but triple coincidences: Mass-mass correlation plot for the two heaviest fragments m_1, m_2 obtained in triple coincidences from ternary decay with the condition $m_1 > m_2 > m_3$ in an order of decreasing masses of the decay partners (see text). Velocities and energies of the corresponding third detected partners do not exceed 0.55 cm/ns and 2 MeV, respectively. The lines are drawn tentatively to guide the eye. See text for more details.

marked by the arrows with the numbers 6, 4, 5, 1, 2, respectively) as those mentioned above in fig. 12. Below the rectangle a horizontal line 3 corresponding to magic ^{98}Sr nucleus is vividly seen. It goes through the thickening of the points 8 centerd at the partition of magic deformed nuclei ^{98}Sr/^{142}Xe. The line $M_s = const = 240$ amu (missing ^{12}C) goes likely through the same point forming the diagonal of the rectangle with the upper left corner at the partition ^{108}Mo/^{132}Sn. The points marked by number 11 lie in the vicinity of the partition corresponding to magic deformed isotopes ^{116}Ru/^{124}Cd (nuclei from the shell minima C′ and K′ in ref. [31]). Lines 9 correspond to missing masses 16 and 24 amu, respectively.

For these data one more peculiarity of the distribution should be mentioned, namely now the region where $M_s > 252$ amu becomes populated. A possible explanation is that a heavy fragment formed in the specific decay mode with, *e.g.*, ^{108}Mo in the exit channel, is followed by a much slower light fragment which, hits the same PIN diode as the previous heavy fragment. The faster fragment defines the TOF. However, the measured energy being the sum of two parts will be incorrect, leading to an incorrect evaluation of the mass of the heavy fragment. A similar situation can appear in the case of ^{144}Ba. Bearing in mind that we really detected three fragments in each event from the distribution in fig. 13 such additional fragment could be the fourth partner of the quaternary decay.

One more remarkable structure consisting of two curves marked by number 10 is connected presumably with a delayed sequential ternary decay. Emition of the light particle provided "start" signal, and results in a population of a shape isomeric state. Later delayed fission of this isomeric state can occur. Both heavy fragments formed have distorted (larger) TOFs and, consequently, increased masses.

A further comment: The velocities and energies of the corresponding lightest central fragments do not exceed 0.55 cm/ns and 2 MeV, respectively. The last number represents also a threshold in the energy channel. Therefore it is not possible to calculate the masses m_3 for the events under discussion.

6 Discussion

With the inclusive data from the new experiments we have confirmed the occurrence of the CCT decay observed previously in ref. [1]. In the neutron gated data we observe new unique rectangular structures bounded by magic clusters in the missing mass data (figs. 9 and 10). We have seen from the COMETA results (figs. 12 and 13), that not only spherical (Ni, Ge) but also deformed magic clusters (^{98}Sr, ^{108}Mo) can be the constituents of such structures.

In this stage of the study of CCT decays we are not ready to propose a detailed physical scenario showing different decay modes and estimate a scenario for the CCT process in the overall picture of cluster effects in nuclei [42–44]. It means that we may have some questionable assignments in the decay channels of the rare CCT process.

With the new experiments, which have a negligible background in arm2 and in arm1, the yield of events in arm1 (facing the source backing) are true missing-mass events (each event is a true coincidence). Additional selection of CCT events in this region has been achieved by the selection with a gate in the V-E space, and in addition with the experimental neutron multiplicities, which implies $Y_{exp-CCT}(n) \gg Y_{bin}(n)$ in some region of the missing-mass space. The neutron source is indeed connected to the ternary fission mode, with differing mass partitions. Keeping in mind the results of sect. 4.2 and 5, we may assume two different sources of neutrons emitted almost isotropically namely from the decaying system before scission (pre-scission neutrons) and from the slow middle fragments of ternary decay. The emission of pre-scission neutrons from the primary nucleus from a strongly deformed shape can be taken as a signature of a complicated fission process.

It has already been stressed that revealing the CCT mode by means of neutron gating is possible only if the neutron sources connected to the CCT and conventional binary fission, respectively, differ by neutron multiplicity or/and their spatial distribution of the neutrons. The latter can enhance the registration of CCT probability due to the geometry of the neutron detectors assembly (neutron belt) used (figs. 2 and 3). Possible differences in the neutron energy spectra are not important, because we have

experimental evidence that two layers of neutron counters in the moderator are enough for the registration of fission neutrons hitting the neutron belt.

Thus we have observed the rectangular structures seen in figs. 9, 10 and 12 due to the fact that with the specific neutron assembly used, the probability $Y_{bin}(n)$ decreases (fig. 8) with the increase of neutron multiplicity (n) in the corresponding region of the mass correlation plot.

Further comments are needed for the evident difference in the structures seen in figs. 9 and 12, respectively, while a similar additional selection gate $n = 3$ was used in both cases. We know (sect. 3.3) that the yield $Y_{phys} \times P_{miss}$ is approximately four times smaller at the COMETA set-up as those at the modified FOBOS spectrometer. At the same time both set-ups have very similar values of P_n (sects. 2.2 and 2.3), *i.e.* $Y_{exp-CCT}(n)$ (formula 2) was less in Ex3 in overall. Keeping in mind that the experimental yield of the different "bumps" increases considerably from the "Ni" bump to "Mo" bump [45] it is understandable why we see only "Mo" bump in Ex3 in the neutron gated data. According to the logic presented, the "Mo" bump must be seen as well in Ex2 within $n = 3$ gate. This is really so, however, we do not show this part in fig. 9b (above the rectangle), because a complicated superposition of different structures are observed there. Additional structures as compared to Ex3 are due to the difference in the blocking mediums in these two experiments.

We comment also on the opening angle of the CCT events and the probability of their registration. We need an opening angle between the two fragments. The major part comes from multiple scattering in the backing (and eventually foils) ref. [36]. The originally collinear fragments can have also a primary (intrinsic) angular divergence. That this value is negligibly small can be deduced from the recently discovered ROT effect [46]. The phenomenon is traced to the rotation of the fissioning nucleus while light particles are ejected. The effect has been observed for the first time in fission of the ^{235}U nucleus induced by cold polarized neutrons. After capture of a polarized cold s-neutron, the $^{236}U^*$ nucleus has the possibility of two spin states 3 and 4, corresponding to two opposite senses of rotation. It was discovered that the angle through which the fission axis rotates and with them the trajectories of α-particles from conventional ternary fission, is very small and barely exceeds $0.2°$. This takes place because the rotation after scission is very short lived and comes to a virtual stop after some 10^{-21} s. due to the drastic increase of the moment of inertia of the system consisting of two fragments flying apart. Thus, even if a di-nuclear system consisting of two CCT partners has an angular momentum of some units of $\hbar$, it is reasonable to expect a situation comparable with the ROT effect, a negligible angular shift between the fission axis of the initial system and that of the di-nuclear system formed after the first rupture.

In general the CCT decay is most likely due to a sequential process with two scissions in a short time sequence. As was shown in ref. [47] the three-body chain-like pre-scission configuration which can lead to the CCT in the frame of such sequential process, is linked to the slopes in the potential energy valley of the decaying system. Evidently this fact explains the much lower yield of the CCT as compared to binary fission which is realized via shapes corresponding to the bottom of the same potential valley. The overall relative yield of 3×10^{-3} contains a large number of mass combinations, as well the enlarged phase space due to higher Q-values and the excited states of the fragments [6].

7 Conclusions

We have performed studies of fission decays of ^{252}Cf, with coincidences of the emitted neutrons in two missing-mass experiments, Ex2 and Ex3. These experiments confirm the observations of the ternary fission process as a collinear cluster tri-partition (CCT), which has been observed in previous experiments (Ex1), described in ref. [1]. The results give new information on the different CCT decay modes (mass partitions):

– The bump discussed earlier in Ex1, ref. [1] does not show a unique combination of ternary masses. Bearing in mind the results presented in figs. 7, 9b, 10, 12, and 13, we observe a sequence of mass partitions. Most structures are based on pairs of magic nuclei, combined with isotopes like $^{128,132}Sn$.

– Specific linear and rectangular structures are observed in Ex2 and Ex3 with increasing neutron multiplicity (shown in figs. 9b, 10, 12). This observation was possible, thanks to a very low background provided by the neutron gating or using mosaics of PIN diodes (with no material in the path of the fragments) in Ex3. These structures provide unique information concerning the evolution of the decaying system near the scission point. Only in this case one can analyse CCT in the multi-dimensional $\{M_1, M_2, V_1, V_2, E_1, E_2\}$ space event by event. In fact, such analysis is impossible in principle for Ex1 with the high background from scattered binary fission events (subtracted by showing the differences of (arm1-arm2)). These events are within the bump observed in fig. 5. The "background" contains also a sum of different CCT modes, and as a whole the sum of CCT components is statistically very significant in the absolute scale.

– It should be emphasized that the yields of the "Ni" bump ($\sim 4 \times 10^{-3}$/binaryFF) and even at heavier masses for the "Mo" bump [45] $\sim 10^{-2}$ per binary fission, are attributed to some tens of different partitions forming in fact the corresponding bump. As was mentioned above the yield of a fixed partition, for instance, $^{68}Ni/^{128}Sn$ (fig. 7) does no exceed $\sim 10^{-5}$/binary fission. Just this yield can reasonably be compared to the probability of known conventional ternary decays with a single light mass isotope emitted.
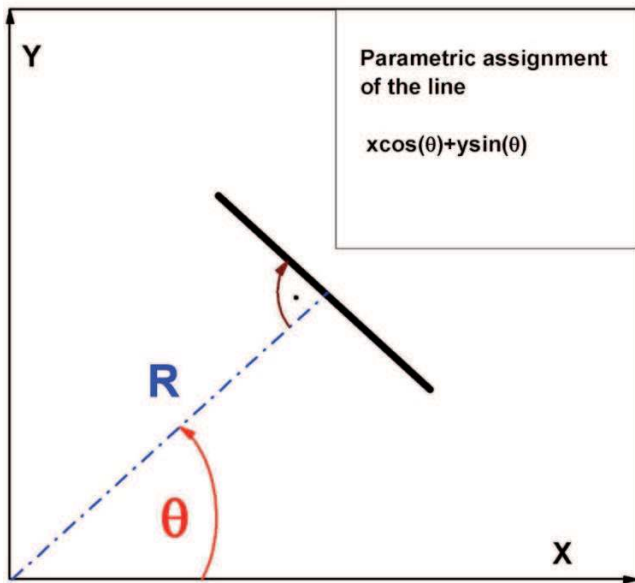
Fig. 14. Parameterization of the line in Hough transform.

Appendix A. Appendix

Appendix A.1. Reliability of linear structures in the scatter plot of fragments masses

Due to the small number of events in the linear structures discussed in figs. 7a, 9, 10, 12, 13 the question arises whether the structures have a physical reality, *i.e.* if they are not a random sequence of points. In order to answer this question a special simulation based on Hough transformation was performed.

The Hough transform is a feature extraction technique used in image analysis, computer vision, and digital image processing [32,33]. The simplest case of Hough transform is the linear transform for detecting straight lines. In the image space, the straight line can be described as $y = mx + b$ and can be graphically plotted for each pair of image points (x, y). In the Hough transform, a main idea is to consider the characteristics of the straight line not as image points x or y, but in terms of its parameters, here the slope parameter m and the intercept parameter b. For computational reasons, it is better to parametricise the lines in the Hough transform with two other parameters, commonly referred to as R and θ (fig. 14).

Actually, the straight line on a plane (fig. 14) can be set as follows:

$$x \times \cos(\theta) + y \times \sin(\theta) = R, \qquad (A.1)$$

where R is the length of the perpendicular lowered on a straight line from the beginning of coordinates, θ is the corner between a perpendicular to a straight line and the axis OX changes within the limits of 0–2π, R are limited by the sizes of the entrance image.

In view of the step-type representation of the entrance data (in the form of a matrix with elements "1" —presence of a point, "0" —its absence), the phase space (R, θ)
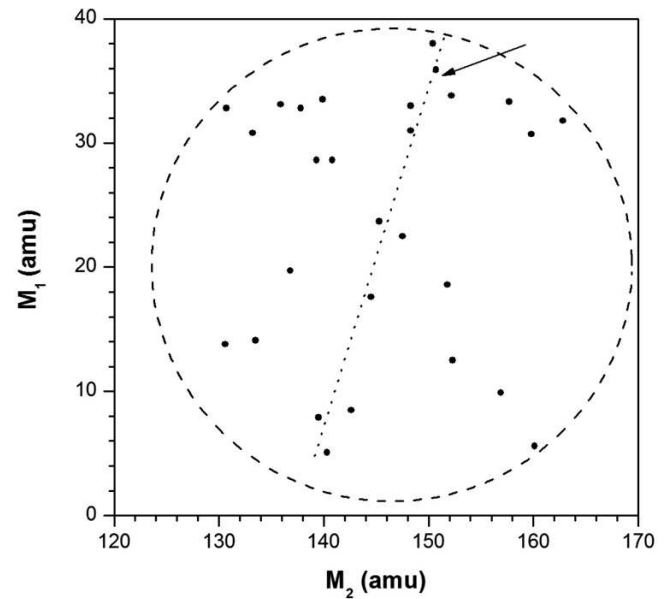

Fig. 15. Part of the distribution shown in fig. 9a chosen for estimation of a reliability of the line structures. Monte Carlo simulation were performed in the circle region marked by the dash line. See text for details.

also is represented in a discrete kind. In this space the grid to which one bin corresponds a set of straight lines with close values of R and θ is entered. For each cell of a grid $(R_i, R_{i+1}) \times (\theta_i, \theta_{i+1})$ (in other words for each Hough transform bin) the number of points with coordinates (x, y), satisfying to the equation is counted up,

$$x \times \cos(\theta) + y \times \sin(\theta) = R, \qquad (A.2)$$

where $\theta_i \leq \theta \leq \theta_{i+1}$, $R_i \leq R \leq R_{i+1}$. The size of bins is obtained empirically.

Beside the steps on R and θ (ΔR, $\Delta \theta$) in the real program code realizing Hough transform, there are the additional parameters responsible for the decision whether all the points, satisfying eq. (A.2), are necessary to attribute an analyzed straight line. So, if the distance in pixels (cells of the matrix under analysis) between extreme points of a line segment is less than the set number n, it is rejected. When the code finds two line segments associated with the same Hough transform bin that are separated by less than the set distance d, it merges them into a single line segment.

A lower part of the scatter plot shown in fig. 10 below $M_1 = 40$ amu was chosen for the analysis (fig. 15). The straight line (marked by the arrow) unite nine points was recognized using Hough transform algorithm at appropriate choice of the principal parameters (ΔR, $\Delta \theta$, n, d).

We tried to estimate the probability of a random realization of the line of such length and tilted to the abscissa axis at an arbitrary angle. A sequence of patterns within randomly distributed points inside was generated. Each circular pattern included precisely the same number of points as those in the initial distribution in fig. 15. An area of circular shape was chosen in order to avoid *a priori* distinguished direction (for instance, diagonal in a rectangular area). Each pattern was processed with the Hough

transform algorithm "tuned" earlier on revealing the line under discussion. Among one hundred patterns analyzed, only two of them provided a positive answer. In other words, a probability of a random realization of the line under discussion is about 2%.

Another approach based on the methods of morphological analysis of images [48,49] was applied as well in order to estimate the probability of random realization of the rectangle seen in fig. 9b. This probability was estimated to be less than 1%.

References

1. Yu.V. Pyatkov *et al.*, Eur. Phys. J. A. **45**, 29 (2010).
2. R.B. Tashkhodjaev *et al.*, Eur. Phys. J. A. **47**, 136 (2011).
3. K. Manimaran *et al.*, Phys. Rev. C. **83**, 034609 (2011).
4. K. Manimaran *et al.*, Eur. Phys. J. A. **45**, 239 (2010).
5. V.I. Zagrebaev *et al.*, Phys. Rev. C. **81**, 044608 (2010).
6. K.R. Vijayaraghavan *et al.*, Eur. Phys. J. A. **48**, 27 (2012).
7. W. von Oertzen *et al.*, Eur. Phys. J. A. **36**, 279 (2008).
8. W. von Oertzen *et al.*, Phys. Rev. C **78**, 044515 (2008).
9. K.R. Vijayaraghavan, W. von Oertzen, K. Manimaran *et al.*, in preparation (2012).
10. C. Wagemans, in *The Nuclear Fission Process*, edited by C. Wagemans (CRS, Boca Raton, 1991) Chapt. 12.
11. E. Piasecki *et al.*, Nucl. Phys. A. **255**, 387 (1975).
12. S.W. Cosper *et al.*, Phys. Rev. **154**, 1193 (1967).
13. H.-G. Ortlepp *et al.*, Nucl. Instrum. Methods A. **403**, 65 (1998).
14. Yu.V. Pyatkov *et al.*, JINR Preprint E15-2004-65, Dubna, 2004.
15. Yu.V. Pyatkov *et al.*, in *Proceedings of the International Conference on Nuclear Physics "Nuclear Shells – 50 Years", Dubna, 1999*, edited by Yu.Ts. Oganessian *et al.* (World Scientific, 2000) p. 301.
16. C. Butz-Jorgensen, H.H. Knitter, Nucl. Phys. **490**, 307 (1988) and references therein.
17. D.V. Kamanin *et al.*, Phys. At. Nuclei **66**, 1655 (2003).
18. S.I. Mulgin *et al.*, Nucl. Instrum. Methods A. **388**, 25 (1997), and references therein.
19. M. Moszynski *et al.*, Nucl. Instrum. Methods. **91**, 73 (1971).
20. Yu.V. Pyatkov *et al.*, in *Proceedings of the 14th International Seminar on Interaction of Neutrons with Nuclei: "Neutron Spectroscopy, Nuclear Structure, Related Topics", Dubna, 2006* (Dubna 2007) p. 134.
21. D.V. Kamanin *et al.*, in *Proceedings of the International Symposium on Exotic Nuclei (EXON-2009), Sochi, 2009*, edited by Yu.E. Penionzhkevich *et al.*, AIP Conf. Proc. (AIP, 2010) p. 385.
22. J.F. Wild *et al.*, Phys. Rev. C. **41**, 640 (1990).
23. D. Rochman *et al.*, Nucl. Phys. A. **735**, 3 (2004).
24. O. Sorlin *et al.*, Phys. Rev. Lett. **88**, 092501 (2002).
25. V. Rao *et al.*, Phys. Rev. C. **9**, 1506 (1974).
26. V. Rao *et al.*, Phys. Rev. C. **19**, 1372 (1979).
27. H. Märton, private communication.
28. F. Gönnenwein *et al.*, Europhys. News **36**, 11 (2005).
29. A.N. Tyukavkin, PhD Thesis, MEPhI, Moscow (2009).
30. MCNP – "Monte Carlo N-Particle code", `http://mcnp-green.lanl.gov`.
31. B.D. Wilkins *et al.*, Phys. Rev. C. **14**, 1832 (1976).
32. `http://en.wikipedia.org/wiki/Hough_transform`.
33. L.G. Shapiro, G.G. Stockman, "Computer Vision", Prentice-Hall, Inc. 2001.
34. N.V. Kornilov *et al.*, Nucl. Phys. A. **789**, 55 (2007).
35. A.S. Vorobyev *et al.*, in *Proceedings of the 17th International Seminar on Interaction of Neutrons with Nuclei: "Neutron Spectroscopy, Nuclear Structure, Related Topics", Dubna, 2009* (Dubna 2010) p. 60.
36. `www.srim.org`.
37. U. Quade *et al.*, Nucl. Phys. A. **487**, 1 (1988).
38. H. Wohlfarth *et al.*, Z. Phys. A. **287**, 153 (1978).
39. J. Henninger, B. Horlbeck, JINR E-6-84-366, Dubna, 1984.
40. D.V. Kamanin *et al.*, in *Proceedings of the 7th International Conference on Dynamical Aspects of Nuclear Fission (DANF-2011), Smolenice castle, 2011*, in press.
41. Y.S. Kim *et al.*, Nucl. Instrum. Methods A. **329**, 403 (1993).
42. D. Poenaru, W. Greiner, *Cluster in Nuclei*, Vol. **1**, edited by C. Beck, *Lect. Notes Phys.*, **818** (2010) p. 1.
43. V. Zagrebaev, W. Greiner, *Cluster in Nuclei*, Vol. **1**, edited by C. Beck, *Lect. Notes Phys.*, **818** (2010) p. 267.
44. G. Adamian *et al.*, *Cluster in Nuclei*, Vol. **2**, edited by C. Beck, *Lect. Notes Phys.*, **848** (2012) p. 165.
45. D.V. Kamanin *et al.*, in *Proceedings of the 18th International Seminar on Interaction of Neutrons with Nuclei: "Neutron Spectroscopy, Nuclear Structure, Related Topics", Dubna, 2010* (Dubna 2011) p. 102.
46. F. Gönnenwein *et al.*, Phys. Lett. B **652**, 13 (2007).
47. Yu.V. Pyatkov *et al.*, Phys. At. Nuclei **66**, 1631 (2003).
48. Yu.P. Pytyev, Pattern Recognition Image Anal. **3**, 19 (1993).
49. Yu.V. Pyatkov *et al.*, Pattern Recognition Image Anal. **20**, 82 (2011).